

Two-Dimensional Wave Number Spectra of Small-Scale Water Surface Waves

BERND JÄHNE

Physical Oceanography Research Division, Scripps Institution of Oceanography, La Jolla, California

KLAUS S. RIEMER

Institut für Umweltphysik, University of Heidelberg, Heidelberg, Federal Republic of Germany

Two-dimensional wave slope spectra have been measured in the large Delft wind-wave facility using an imaging optical technique and digital image processing. The data cover wavelengths from 0.4 to 24 cm and wind speeds (U_{10}) from 2.7 to 17.2 ms^{-1} . The spectral densities of small gravity waves at higher wind speeds are proportional to $k^{-3.5}$ and u_* . Capillary-gravity and capillary waves show features which clearly manifest that the energy balance for these waves is much different from that for gravity waves. The degree of saturation is approximately constant at a given wind speed, but strongly increases with friction velocity ($\propto u_*^{2.5}$). A sharp cutoff, which is almost independent of the wind speed, occurs at a wavelength of about 7 mm.

1. INTRODUCTION

The complex two-dimensional propagation and interaction of small-scale wind waves on the ocean surface cannot adequately be measured with point measuring devices such as wire and laser slope gauges. Such instruments yield time series from which only the temporal characteristics can be derived. No insight is gained into the two-dimensional spatial structures of the wave field.

A more detailed knowledge of these properties, however, is crucial for a deeper understanding of small-scale air-sea interaction processes and active remote sensing of them with microwaves. From scale considerations it is clear, whatever the detailed mechanisms may be, that backscatter of electromagnetic waves is determined by structures on the water surface of the same scale as the incident wavelengths, i. e., by small-scale waves in the capillary-gravity range with wavelengths ranging from centimeters to millimeters.

The dependency of these small wavelets on the wind speed and friction velocity, is the basis of remote sensing of the wind speed and direction by measuring the radar backscatter cross section [Schroeder *et al.*, 1982; de Loor, 1983]. Yet, the mean spectral densities of the small-scale waves also depend on a number of other parameter as derived by recent studies of the radar backscatter. Keller *et al.* [1985] found a significant increase in the radar return with increasing atmospheric instability. Another important factor is the development of the wave field commonly expressed in the nondimensional wave age. Wind speeds determined by scatterometers and altimeters are considerably overestimated at high wave ages [Glazman *et al.*, 1988; Glazman

and Pilorz, 1990]. Furthermore, surface active films significantly damp even small gravity waves with frequencies as low as 2 Hz [Alpers and Hühnerfuss, 1989].

Of equal importance is the modulation of the small-scale waves by larger-scale features such as large-scale gravity waves, internal waves, tidal currents, and bottom topography [Komen and Oost, 1989]. Through these interactions, large-scale features can be made visible by imaging radar systems such as synthetic aperture radars (SAR).

A more detailed investigation of all these effects depends entirely on knowledge of the small-scale structures on the sea surface. There are virtually no laboratory and at-sea measurements of wave number spectra available for waves in the capillary-gravity and capillary range. Previously published measurements are limited to larger wavelengths and include rather sporadic and limited data, but no systematic study over a wide range of parameters.

Banner *et al.* [1989] report wave number spectra based on stereophotogrammetric determination. Their measurements were obtained from an oil platform and covered a wavelength range from 0.2 to 1.6 m and wind speeds from 7 to 13.3 ms^{-1} . Because of the coarse resolution of only 33×33 pixels, only one-dimensional wave number spectra, i. e., projections of the two-dimensional spectra are discussed.

During the TOWARD experiment, Shemdin *et al.* [1988] also used stereophotography to derive two-dimensional wave number spectra. The stereo images were taken from an image sector of 2.5 m \times 2.5 m and were evaluated manually with a resolution of about 300×300 pixels. The wave number spectra, calculated from 8-10 frames per condition, include wavelengths between 0.02 and 1 m and cover wind speeds from 1.5-5.0 ms^{-1} .

The results of these two investigations disagree: While Shemdin *et al.* [1988] found that the spectral densities go with $k^{-3.6}$ and increase with wind speed, Banner

Copyright 1990 by the American Geophysical Union.

Paper number 90JC00510
0148-0227/90/90JC-00510\$05.00

et al. [1989] obtained a $k^{-4.0}$ dependency and no significant change with wind speed. For further interpretation, more data are needed since both papers include only a few spectra. Furthermore, the wind speed ranges of the investigations do not overlap.

Very recently, in the course of the SAXON-I field experiment at the Chesapeake Light Tower, stereo and Stilwell-type [Stilwell, 1969] image sequences have been taken [Shemdin and McCormick, 1989]. Thus, in the near future more field data should be available. However, the new data will not include capillary waves, since it is estimated that only waves down to wavelengths of 1 cm and 2 cm will be resolved with the stereo and Stilwell technique, respectively.

In conclusion, considerable progress in the experimental technique and data analysis of wave images is still necessary to produce instruments which (1) can resolve the smallest wave scales; (2) can operate under a wide range of conditions in the field; and (3) allow a systematic study of the spatial wave characteristics.

We chose a step by step approach to this difficult matter, starting with the relative easy indoor environment of a wind/wave facility and going to the much more demanding environment at sea. This seems to be the most efficient way to develop the measuring technique. A description of the optical wave measuring technique envisaged is given by Jähne and Waas [1989].

The experiments reported in this paper were performed in the well-controlled indoor Delft wind/wave facility within the first phase of the VIERS project, an international and multidisciplinary cooperation to forward the understanding of microwave backscattering and small-scale water surface waves [van Halsema *et al.*, 1989]. The measuring program focused on synchronous recording of the backscatter cross section with an X-Band FM/CW radar (9.6 GHz) and of wave image sequences at the same footprint on the water surface (van Halsema *et al.*, in preparation, 1990)

Meanwhile, a second experiment took place in March 1989 in the even larger outdoor 250 m long and 5 m deep Delta flume, where full-scale gravity waves could be generated. As last step, an experiment is planned from the Noordwijk research platform in the North Sea.

This paper discusses two-dimensional wave number spectra and consists of four sections: The first section briefly discusses the present theoretical knowledge about wave number spectra of small-scale waves. Sections 3 and 4 cover the experimental techniques and the processing of the wave images. The experimental results are discussed in section 5.

2. SLOPE WAVE NUMBER SPECTRA

2.1. Wave Slope

Since we performed wave slope measurements, we start with a discussion of the wave slope and its relation to the wave height. The wave slope is the gradient of the water surface deflection $a(\mathbf{x}, t)$

$$\mathbf{s}(\mathbf{x}, t) = \nabla a(\mathbf{x}, t). \quad (1)$$

It is a two-dimensional vector function with two components, the along-wind component, s_1 , and the cross-wind component, s_2 . The relation between the slope

and amplitude power spectra can easily be deduced from the Fourier transform of the water surface deflection

$$\hat{a}(\mathbf{k}, \omega) = \int_{x_1} \int_{x_2} \int_t a(\mathbf{x}, t) \exp[-i(\mathbf{k}\mathbf{x} - \omega t)] d\mathbf{x} dt, \quad (2)$$

where $\hat{a}(\mathbf{k}, \omega)$ is the complex-valued amplitude function. The slope spectra (along-wind S_1 , cross-wind S_2 , and total $S = S_1 + S_2$ as the sum of both) are given by

$$\begin{aligned} S_1 &= k_1^2 |\hat{a}(\mathbf{k}, \omega)|^2 = k^2 \cos^2 \Theta A(\mathbf{k}, \omega) \\ S_2 &= k_2^2 |\hat{a}(\mathbf{k}, \omega)|^2 = k^2 \sin^2 \Theta A(\mathbf{k}, \omega) \\ S &= k^2 |\hat{a}(\mathbf{k}, \omega)|^2 = k^2 A(\mathbf{k}, \omega) \end{aligned} \quad (3)$$

where $\hat{A}(\mathbf{k}, \omega) = |\hat{a}(\mathbf{k}, \omega)|^2$ is the directional wave number-frequency spectrum of the wave amplitude and Θ the angle between the wind direction and the propagation direction of the wave.

2.2. Wave Number Spectra

Single images of the waves on the water surface yield only the spatial structures and thus only wave number spectra can be calculated. The wave number spectra are obtained from the directional wave number-frequency spectrum by integration over all frequencies contributing to a single wave number, i. e., by a projection of the 3-D spectrum onto the wave number plane.

$$\begin{aligned} F(\mathbf{k}) &= \int_{\omega} \hat{A}(\mathbf{k}, \omega) d\omega \\ S_1(\mathbf{k}) &= k^2 \cos^2 \Theta \int_{\omega} \hat{A}(\mathbf{k}, \omega) d\omega \\ S_2(\mathbf{k}) &= k^2 \sin^2 \Theta \int_{\omega} \hat{A}(\mathbf{k}, \omega) d\omega \\ S(\mathbf{k}) &= k^2 \int_{\omega} \hat{A}(\mathbf{k}, \omega) d\omega, \end{aligned} \quad (4)$$

These relations mean that the total slope wave number spectrum S can directly be derived from the height wave number spectrum F and vice versa:

$$F(\mathbf{k}) = k^{-2} S(\mathbf{k}), \quad S(\mathbf{k}) = k^2 F(\mathbf{k}) \quad (5)$$

This relation gives free choice to measure either the slope or the height of the waves. If slope measurements are chosen, it is important to measure the total slope spectrum, i. e. both the along- and cross-wind components. If only one component is available, waves traveling perpendicularly to the corresponding direction do not contribute to the spectral densities and are lost because of the angular weighting factors $\cos^2 \Theta$ and $\sin^2 \Theta$ for along- and cross-wind components (4).

2.3. Saturation Range and Representation of Spectra

The simplest concept of an upper-limit asymptote of the spectrum, the saturation range, goes back to the early work of Phillips [1958]. He postulated that dissipation (e. g., by wave breaking) imposes an upper limit on the spectral densities. If this limit is independent of the energy input by the wind and depends only on the

restoring gravity and capillary forces, g and $\gamma = \sigma/\rho$, respectively, (σ denotes the surface tension) a simple dimensional analysis

$$\begin{aligned} [F(\mathbf{k})] &= L^{-4} & [S(\mathbf{k})] &= L^{-2} \\ [g] &= LT^{-2} & [\gamma] &= L^3T^{-2} \end{aligned} \quad (6)$$

yields

$$\begin{aligned} F(\mathbf{k}) &= \beta f(\Theta)k^{-4} \\ S(\mathbf{k}) &= \beta f(\Theta)k^{-2} \\ S_1(\mathbf{k}) &= \beta \cos^2 \Theta f(\Theta)k^{-2} \\ S_2(\mathbf{k}) &= \beta \sin^2 \Theta f(\Theta)k^{-2} \end{aligned} \quad (7)$$

where the dimensionless function $f(\Theta)$ describes the angular spread of the waves, which, of course, cannot be derived from dimensional analysis alone. Since the saturation range does not explicitly depend on the restoring force, the wave number spectra for capillary and gravity waves show the same spectral shape, although the constant β may be different.

The saturation spectrum (7) corresponds to a wave field which, statistically, shows spatial discontinuities in the slope, i. e., the first spatial derivative. This simple fact emphasizes that the slope is a basic parameter for the waves. Indeed, the slope of the wave is the parameter which describes the nonlinearity of waves in the Navier-Stokes differential equation [Kinsman, 1965]. From the experimental point of view, slope measurements offer a significant advantage over height measurements since the slope signal has a much smaller dynamic range. Clearly, the concept of a saturation range is an oversimplification. It is very helpful, however, in representing spectral densities. All spectra in this paper are represented as a dimensionless function, the "degree of saturation" $B(\mathbf{k})$, as proposed by Phillips [1985]

$$B(\mathbf{k}) = F(\mathbf{k})k^4 = S(\mathbf{k})k^2 \quad (8)$$

A different train of thought leads to the same representation for wave spectra. The starting point is the fact that real-world data are obtained from discrete grids. A Cartesian wave number grid, which results from the discrete Fourier transform of an image, is not an optimum choice. The relative wave number resolution in the wave spectra is not constant, but increases proportional to the wave number to unnecessarily high levels well below 1%. Moreover, it is costly and cumbersome to extract the angular dispersion, profiles in a certain direction, or the dependency of the spectral density on the absolute wave number from the Cartesian grid.

These demands are much better met by a discrete grid in a $(\ln k, \Theta)$ space, which preserves a constant relative k resolution and allows easy extraction of the angular dispersion and k profiles. Actually, these features are directly visible in such a representation, while it is hardly possible to compare angular dispersions of different wave numbers in a Cartesian grid. The transition from a (k_x, k_y) grid to the $(\ln k, \Theta)$ grid for the spectral densities is given by

$$S(\mathbf{k})dk_1dk_2 = S'(\mathbf{k})d \ln k d\Theta \quad (9)$$

Using $dk_1 = k d\Theta$, $dk_2 = k d \ln k$ and (8) yields

$$S'(k, \Theta) = k^2 S(k, \Theta) = B(k) \quad (10)$$

On a $(\ln k, \Theta)$ grid the slope spectrum is directly expressed as the degree of saturation B . The multiplication by k^2 reflects the fact that the area of the grid cells increases with k^2 . Representation of the wave number spectra in a $(\ln k, \Theta)$ grid, instead of a Cartesian grid, also yields considerable data compression.

2.4. Energy Balance in Small-Scale Waves

The key to a deeper understanding of the wave spectra lies in the determination of the energy balance of the waves. In a stationary wave field, the spectral densities adjust in such a way that the different sources and sinks balance each other in the mean. Basically there are three terms [Phillips, 1985]: (1) energy input by the turbulent wind field; (2) transfer of energy between waves of different wave numbers by nonlinear wave-wave interaction; and (3) dissipation of energy by wave breaking, viscous dissipation, and turbulent diffusion.

Even for small gravity waves there is a considerable lack of knowledge. While the input of energy by wind is known best, the mechanisms and magnitude of the wave dissipation term is quite uncertain [Plant, 1989]. Recently, two models have been proposed, both yielding an increase in the degree of saturation with $k^{1/2}$ and u_* on quite different assumptions. Phillips [1985] assumed that all three fluxes sketched above are of equal importance. Balancing these terms locally, he obtained

$$\begin{aligned} F(\mathbf{k}) &= \beta g^{-1/2} f(\Theta) u_* k^{-7/2} \\ B(\mathbf{k}) &= \beta g^{-1/2} f(\Theta) u_* k^{1/2} \end{aligned} \quad (11)$$

In contrast, Kitaigorodskii [1983] proposed the existence of a Kolmogoroff-type energy cascade in which the wind input primarily occurs at the energy-containing large scales and dissipation at small scales. As a consequence, the spectral energy flux in the intermediate wave numbers is constant, and he also obtained (11).

For capillary-gravity and capillary waves, several new aspects, which make a theoretical treatment of the energy balance even more difficult, come into play:

Strong nonlinear wave-wave interaction. Resonant nonlinear wave-wave interaction in the gravity range takes place between quartets of waves. This is a "weak" process in the sense that the characteristic time scale is hundreds of wave cycles [Kinsman, 1965]. In contrast, resonant interactions between capillary-gravity waves occur in triplets and are much stronger; the third wave component is excited in less than five cycles of the interacting waves [McGoldrick, 1965].

Energy transfer over a wide range of wave numbers. Steep gravity waves generate ripples at their crests. This mechanism transfers energy over a wide wave number range. In contrast the standard perturbation theory for nonlinear wave-wave interaction deals only with waves of similar wavelengths. To the knowledge of the authors, no estimates are available comparing these different modes of energy transfer.

Viscous cutoff. Towards high wave numbers, viscous dissipation should become dominant, since it is proportional to the wave number squared [Phillips, 1980]. It is generally believed that viscous dissipation sets the upper limit for waves which can be generated on the water surface. In order to estimate the viscous cutoff, Donelan

and Pierson [1987] balanced the wind input and viscous dissipation term and argued that wave numbers for which the wind input term is smaller than the viscous dissipation can not be generated. Their calculations (Figure 4 of their paper) lead to a cutoff wave number which strongly increases with the wind speed, due to an increase of the wind input term, and less strongly with temperature, due to a decrease of the kinematic viscosity. The cutoff wave numbers range from about 200 m^{-1} ($\lambda = 3 \text{ cm}$) at 2.7 ms^{-1} wind speed to about 1100 m^{-1} ($\lambda = 0.57 \text{ cm}$) at 12 ms^{-1} .

Turbulent wave dissipation and interaction with shear currents. A closer review of this term is lacking. Only recently, Rosenthal [1989] proposed that turbulent diffusion yields a nonlinear mechanism for wave dissipation which agrees in the order of magnitude with the measured spectral densities. Damping of capillary waves by turbulence is, of course, governed by eddies of much smaller scales. The damping mechanisms may be quite different, since the penetration depth of these waves, $\lambda/2\pi$, is of the same order as the wind driven shear current in the viscous boundary layer. Thus, these waves propagate in a strongly sheared layer. These effects became important in research on air-sea gas exchange, in order to explain the strong enhancement of the air-sea gas transfer rate in the presence of waves [Jähne *et al.*, 1987]. Since the gas transfer is controlled by a layer which is considerably thinner than the aqueous viscous boundary layer, it is a sensitive indicator for turbulence very close to the water surface.

Surface films. Besides wave breaking, viscous and turbulent dissipation, waves are also dissipated by monomolecular surface films. This fact makes the wave field dependent on a variety of chemical and biological parameters. Despite this complexity, the basic relations between the damping factor and the viscoelastic properties of the surface films are well established [Alpers and Hühnerfuss, 1989].

The many parameters influencing small-scale waves are a challenge for more detailed measurements. Such experimental data could help to sort out predominant mechanisms and to guide further theoretical research.

3. EXPERIMENTAL TECHNIQUE

3.1. Slope Measurements by Light Refraction

The imaging of the wave slope is based on light refraction at the water surface. The same principle has been used for laser slope gauges [Cox, 1958; Tober *et al.*, 1973; Hughes *et al.*, 1977; Lange *et al.*, 1982; Jähne, 1989b; Jähne and Waas, 1989]. The water surface is observed by a CCD camera mounted at the ceiling of the facility, 4 m above the water level.

A submerged illumination system similar to the device constructed by Keller and Gotwols [1983] is used. It was modified to visualize both the along- and cross-wind slopes of the waves (compare section 2.2.). It replaces one of the $2 \text{ m} \times 2 \text{ m} \times 0.3 \text{ m}$ concrete plates which cover the bottom of the end section of the water channel in the Delft facility (Figure 1). The illumination system fits smoothly into the bottom of the facility and does not cause any disturbance of the flow and waves in the water tank.

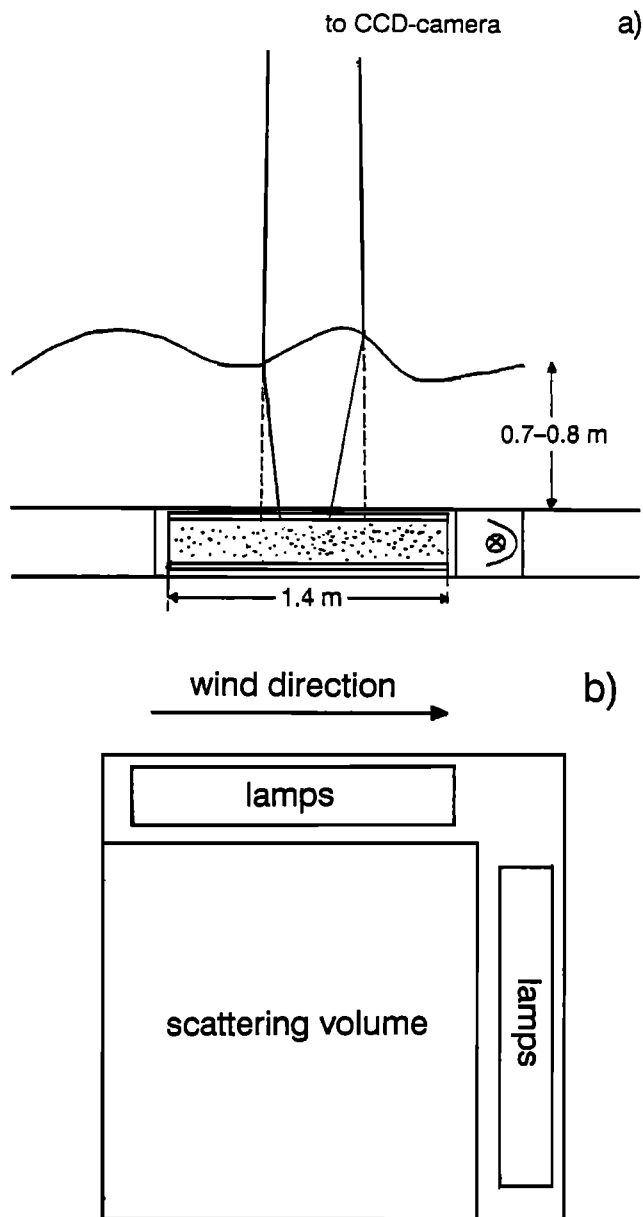


Fig. 1. Setup of the imaging slope gauge in the Delft wind-wave facility: (a) cross section in wind direction; (b) view of the submerged illumination system from above.

A row of six 150-W Osram HQI metal vapor lamps is located at the down- and cross-wind side walls of a $1.4 \text{ m} \times 1.4 \text{ m} \times 0.2 \text{ m}$ glass box containing an aqueous suspension of Dow Latex particles with a diameter of $0.4 \mu\text{m}$ (Serva Feinbiochemica). The particles are used to scatter the light in the box. Double glass windows at the bottom and top of the scattering volume act as a light guide by total reflection. Only one of the two rows of lamps is used at a time. This simple setup should — according to first-order scattering theory — result in an exponential decrease of the brightness I in the direction perpendicular to the corresponding row of lamps

$$I(X) = I_0 \exp(-X/\bar{X}) \quad (12)$$

If the water surface is flat, the CCD camera observes a

horizontally or vertically changing intensity. The measured profiles show close agreement. The along-wind profile (Figure 2a) is approximately exponential, with \bar{X} being roughly equal to the illuminated width of the image, while the cross-wind profile is constant (Figure 2b). When the water surface is inclined by waves, the light beam received by the CCD-camera comes from a place in the illumination source which is more or less bright. In this way, the intensity gradient is modulated by the slope of the waves.

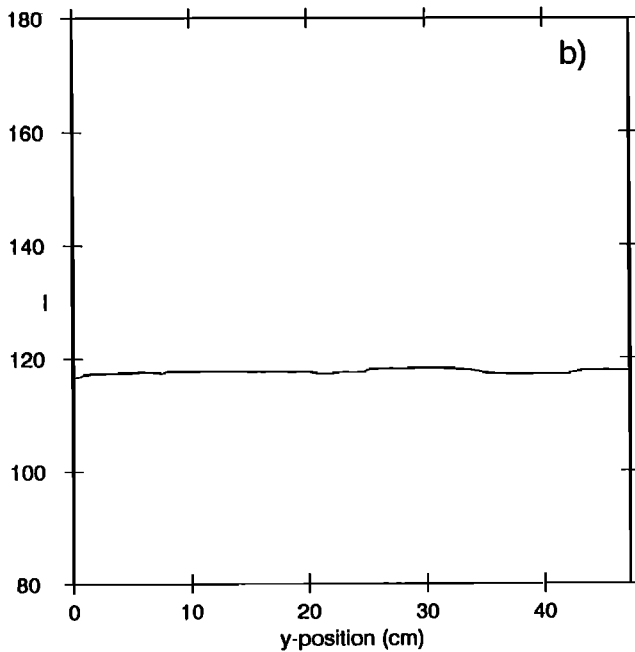
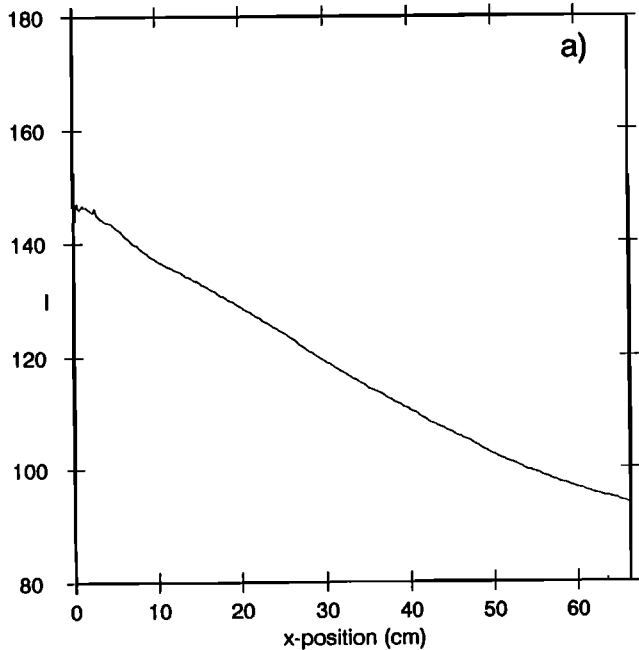


Fig. 2. Intensity profile of the image for a flat water surface with an along-wind illumination gradient: (a) along-wind profile; (b) cross-wind profile.

It is important to note that focusing and defocusing caused by the lens effects of surface curvature cannot occur with this setup. The "ripple at the bottom of the tank effect" is only observed when a bundle of parallel light or convergent light, emitted from a point source, illuminates the water surface. The illumination source used in the imaging slope gauge is quite different. It is large, and the light is emitted in a wide cone, limited only by total reflection at the glass-air interface at the upper double glass window of the scattering volume. It is shown below that the illumination cone is wide enough even for high wave slopes.

3.2. Wave Slope and Image Intensity

A quantitative relation between the intensity modulation and the wave slope can be derived by ray tracing (Figure 3) assuming that the light source radiates light

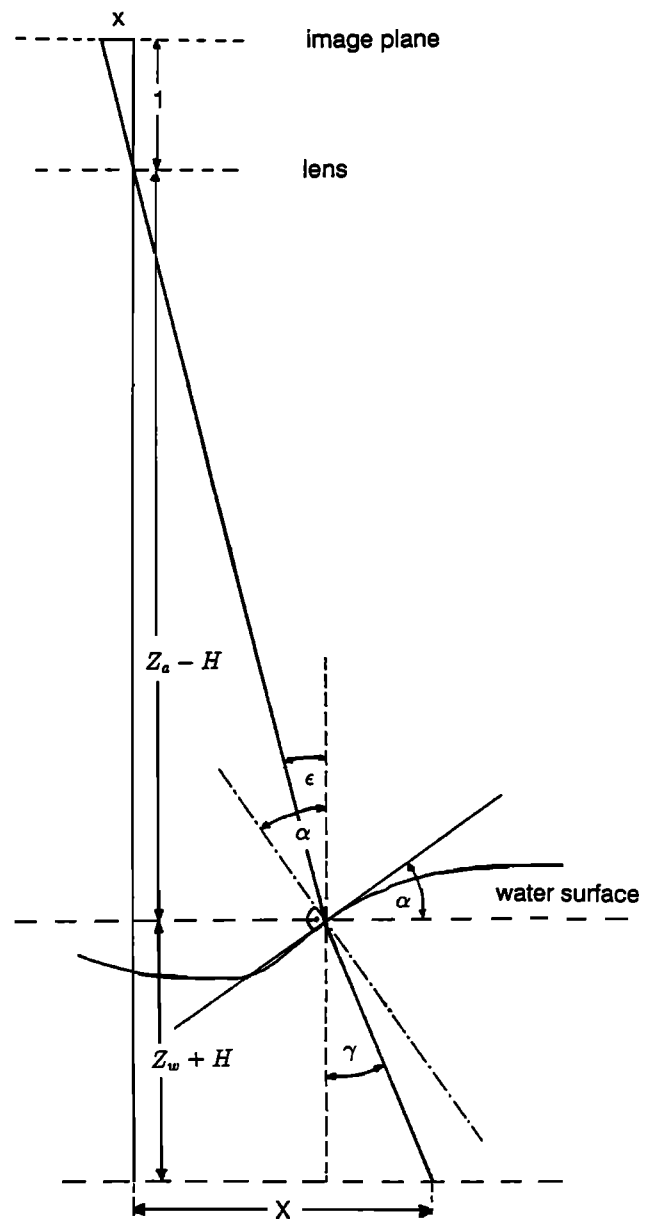


Fig. 3. Optical geometry of the imaging wave slope gauge.

isotropically in all directions. In the following considerations emphasis is put on a careful estimate of the various nonlinearities related to the refraction law and the exponential intensity profile.

For the sake of simplicity, dimensionless coordinates $(x, y) = (\tan \epsilon_1, \tan \epsilon_2)$ are used to denote the position on the image plane. Three-dimensional world coordinates are indicated by capital letters (X, Y, Z) . The optical axis of the system is aligned along the Z axis.

The horizontal position (X, Y) in the light source corresponding to a point (x, y) on the image plane is then given by (compare Figure 3)

$$\begin{pmatrix} X \\ Y \end{pmatrix} = (Z_a - H) \begin{pmatrix} x \\ y \end{pmatrix} + (Z_w + H) \begin{pmatrix} \tan \gamma_1 \\ \tan \gamma_2 \end{pmatrix} \quad (13)$$

where Z_a and Z_w are the distances from the camera to the mean water level and from the mean water level to the light source, respectively, and H is the wave height. Since the intensity changes in only one direction, we need to consider only one component of (13); we take the along-wind component.

Next, the relation between the slope $s_1 = \tan \alpha_1$ of the water surface and the refraction angle γ_1 is considered in order to eliminate γ_1 from (13) (Figure 3). Elementary trigonometry and the law of refraction yield

$$s_1 = \tan \alpha_1 = \frac{n_w \sin \gamma_1}{n_w \cos \gamma_1 - \cos \epsilon_1} - \frac{\sin \epsilon_1}{n_w \cos \gamma_1 - \cos \epsilon_1} \quad (14)$$

Introducing the image coordinate $x = \tan \epsilon_1$ yields

$$s_1 = \sqrt{1+x^2} \left(\frac{n_w \tan \gamma_1}{n_w \sqrt{1+x^2} - \sqrt{1+\tan^2 \gamma_1}} - \frac{x \sqrt{1+\tan^2 \gamma_1}}{n_w(1+x^2) - \sqrt{1+\tan^2 \gamma_1}} \right) \quad (15)$$

Clearly, the dependence of $\tan \gamma_1$ on the wave slope s_1 and the image coordinate x is nonlinear. A third-order Taylor expansion in x and $\tan \gamma_1$ yields the following approximation after some lengthy calculations (using $n_w = 4/3$)

$$\tan \gamma_1 = \frac{1}{4}s_1 \left[1 + \frac{3}{2}x^2 - \frac{3}{32}(s_1 + 3x)^2 \right] + \frac{3}{4}x \left[1 - 2x^2 - \frac{5}{32}(s_1 + 3x)^2 \right] \quad (16)$$

The refraction angle γ_1 equals only about a quarter of the wave slope (if $s_1 = 1, \gamma_1 = 13^\circ$). Thus γ_1 covers only a small range. Consequently, the use of the Taylor expansion in $\tan \gamma_1$ and the assumption of an isotropic light source (section 3.1.) are justified. Substituting this equation into (13) yields X as a function of the wave slope s_1 and the position in the image plane x

$$X = (Z_a - H)x + \frac{Z_w + H}{4} \left\{ s_1 \left[1 + \frac{3}{2}x^2 - \frac{3}{32}(s_1 + 3x)^2 \right] + \frac{3}{4}x \left[1 - 2x^2 - \frac{5}{32}(s_1 + 3x)^2 \right] \right\} \quad (17)$$

The shift in position of the illumination source ΔX from a flat water surface ($s_1 = H = 0$) to a wavy surface is given by

$$\Delta X = \frac{Z_w + H}{4} s_1 \left[1 + \frac{21}{32}x^2 - \frac{3}{32}s_1^2 - \frac{9}{16}s_1 x \right] - \frac{H}{4}x - \frac{3Z_w}{4}x \left[\frac{5}{32}s_1^2 + \frac{30}{32}s_1 x \right] \quad (18)$$

The shift in position ΔX is essentially proportional to the wave slope s_1 . The wave height H causes a sensitivity shift. Ripples at the crest of large waves are imaged more sensitively than at the trough. In our experiments with pure wind waves, the wave height was at most 5 cm. Since the mean distance to the light source was 85 cm, the effect is only about 6%. The effect on mean wave number spectra is much less, since only an uneven distribution of the ripples would cause a bias in spectral densities.

Equation (18) contains the effects of the nonlinearity related to the refraction law. These effects are of third order in the wave slope s_1 and the image coordinate x . In order to reduce the nonlinearities, it is essential to keep x small, i.e., by putting the camera as far away from the water surface as possible. In our setup, x was always smaller than 0.1. Then the position-dependent nonlinearities are 6.2% for $s_1 = 1$ and 2.3% for $s_1 = 0.3$ at the edges of the image. In the mean, the effects are much lower, since the largest term $3/32s_1x$ is linear in the position and thus cancels when integrated over the whole image. A bias of only 0.3%, which is caused by the term quadratic in x , remains. The nonlinearities which depend only on the wave slope are larger. The slope signal is 9.4% and 0.8% lower than expected from a linear relation for $s_1 = 1$ and $s_1 = 0.3$, respectively.

The second term in (18) causes a zero-point shift for the slope signal. The effects are small and therefore negligible. A wave height of 5 cm causes a slope shift of 0.0063 at the edge of the image. The position-dependent shift is 0.028 and 0.009 at the edge of the image for slopes of 1 and 0.3, respectively, while the slope itself results in a zero shift of 0.047 and 0.004, respectively.

Finally, the intensity change is related to the wave slope by expanding (12) in a Taylor series, using (18) to substitute ΔX

$$\Delta I = I(s) - I(0) = -\alpha I(0)s_1$$

$$\left[1 - \frac{1}{2}\alpha s_1 + \left(\frac{1}{6}\alpha^2 - \frac{3}{32} \right) s_1^2 - \frac{9}{16}s_1 x \right] \quad (19)$$

with

$$\alpha = \frac{Z_w + H}{4X} \quad (20)$$

$I(0)$ denotes the intensity which would be obtained for a flat water surface at the same point. The exponential intensity profile introduces a quadratic nonlinearity into the slope/intensity relation. However, the effects on the wave number spectra are small. As an example for a wave with $s_1 = 0.5$, a secondary peak will show up in the spectrum at twice the wave number with an

amplitude of only 0.4% of the spectral density at the actual wave number. Even if the slope spectrum drops rapidly with the wave number, say proportional to k^{-4} , the spectral densities will only be in error by 6%.

Summarizing, we can say that the slight nonlinearities of the whole system do not affect the spectral densities to such an extent that it would be worthwhile to correct them. Likewise, it is not necessary to compensate for the sensitivity decrease proportional to the intensity $I(0)$ in (19), since it acts as a windowing function which is applied to the images anyway, before performing the Fourier transform (see section 4.3.).

Though only either the along- or cross-wind slope of the waves is made visible, the images contain the directionality of the waves. A wave with the slope s_0 traveling at an angle Θ to the wind speed direction, shows along- and cross-wind slope components, $s_0 \cos \Theta$ and $s_0 \sin \Theta$, respectively. In an angular sector of $\pm 60^\circ$ the amplitude damping in the corresponding slope signal is less than a factor of 2.

3.3. Image Acquisition and Digitization

The images were acquired with a Siemens K230 interline transfer CCD camera. In order to obtain sharp images, the exposure time was limited to 1.7 ms by a chopper wheel rotating in front of the camera lens synchronously with the video signal. During the experiments the wave image sequences were recorded on a Umatic video tape recorder.

The images were digitized with a spatial resolution of 512×512 pixels and 256 grey values (one byte per pixel), using an Imaging Technology FG100 image processing board in a 10 MHz PC-AT compatible personal computer. Since a full frame consists of two half frames which are individually illuminated with a time difference of 20 ms, only half frames with a horizontal (along-wind) and vertical (cross-wind) resolution of 512 and 256 pixels, respectively, were processed. The further features of the digitized images are summarized in Table 1.

3.4. Spatial Resolution

The spatial resolution of the images is limited by two effects. The first factor is the overall spatial transfer function of the electro-optical system from the camera lens, the CCD chip, and the videorecorder to the video signal processing prior to digitization. Measurements with test images containing fine lines yielded a steep cutoff at a wave number of 1250 m^{-1} , which is slightly more than half of the Nyquist wave number k_0 (Table 1). The second factor is the blurring of the images by the motion of the waves. If it is assumed that the intensity is constant during the exposure time Δt , the

wave image sequence $s(\mathbf{x}, t)$ is convolved along the time coordinate with a rectangular function Π of the width Δt .

$$s'(\mathbf{x}, t) = s(\mathbf{x}, t) * \Pi\left(\frac{t}{\Delta t}\right) \tag{21}$$

Consequently, the frequency spectrum is multiplied by the Fourier transform of Π , the sinc-function

$$\hat{s}'(\mathbf{k}, \omega) = \hat{s}(\mathbf{k}, \omega) \cdot \frac{\sin(\pi \Delta t \nu)}{\pi \Delta t \nu} \tag{22}$$

The sinc-function falls off to one half at a frequency $\nu_c \approx 0.6033/\Delta t$, which reduces to 355 Hz for the chosen exposure time of 1.7 ms. Even if we assume phase velocities as large as 1 ms^{-1} for these small waves (by advection with the orbital velocities of large waves), the corresponding wave number cutoff starts only at 2230 m^{-1} , which is just about the along-wind Nyquist wave number.

These simple estimates are supported well by measurements made without the mechanical chopper, i.e., an exposure time of 40 ms. The observed cutoff in the spectral densities was found to be in good agreement with (22).

It can be concluded that the spatial resolution is limited rather by the total transfer function of the setup than by the velocity smearing. Waves down to a wavelength of 0.5 cm can be measured without significant damping.

3.5. Calibration

The imaging slope gauge was calibrated with a "frozen wave" built from a thin transparent foil, which was bent into a sinusoidal shape by a surrounding frame. The whole device is put onto the water surface in such a way that the space below the foil is filled with water. This calibration wave has a wavelength of $0.130 \pm 0.002 \text{ m}$

TABLE 1. Summary of the Features of the Digitized Wave Images

Feature	Horizontal Direction (Along-Wind)	Vertical Direction (Cross-Wind)
Size	66.35 cm	47.28 cm
Pixels	512	256
Spatial resolution	1.30 mm	1.85 mm
Maximum wave number	2424 m^{-1}	1701 m^{-1}

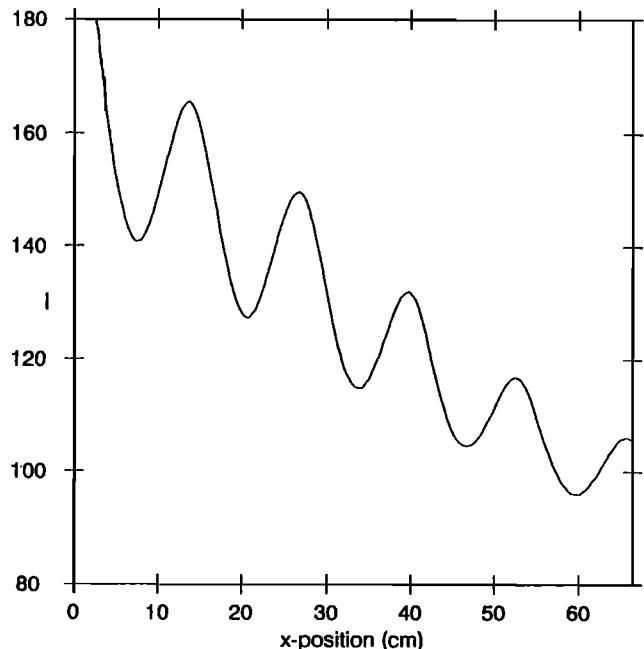


Fig. 4. Intensity profile of the calibration object, an artificial wave with $\lambda = 13 \text{ cm}$ and a slope amplitude $s_0 = 0.484$. The wave and the illumination gradient are oriented along-wind.

and a slope amplitude of $0.484 \pm 5\%$. Its size of $74 \text{ cm} \times 103 \text{ cm}$ is large enough to fit into the largest sector to be measured. Figure 4 shows an intensity profile averaged over all lines with the wave aligned in the along-wind direction.

3.6. Nonlinearity

The overall nonlinearity of the imaging slope gauge was estimated by processing a sequence of images with the sinusoidal calibration wave. The second and third harmonics were found to be 0.3% and 0.018%, respectively, of the spectral densities of the main peak in the power spectra, which is in good agreement with the estimates discussed in section 3.1.

3.7. Noise Level

Data obtained as images contain only a low dynamic range because of the limited resolution, typically 8 bits. Thus, the information is easily corrupted by noise or artifacts in the images. Besides the electronic noise of the imaging CCD sensor, the video recording equipment, and the video analog-digital converter, there is another noise source, which is very difficult to handle: small particles floating in the water and sedimenting onto the glass plate of the illumination source. As long as parts of the water surface are flat, these particles become visible and increase the noise level. When the water surface becomes rough they are no longer visible. Thus this noise source is signal-dependent and unpredictable. Consequently, the detection of ripples with low slopes at low wind speeds is the most critical issue. It turned out that the most reliable indicator is a direct comparison of the wave number spectra with the slope frequency spectra simultaneously obtained with the laser slope gauge (see section 5.2.).

Another problem is fixed patterns in the images. Even faint patterns which are not detectable by eye, can cause spikes in the spectrum. We observed spurious sensitivity changes from line to line in the image which resulted in peaks in the spectrum in the cross-wind direction.

4. WAVE IMAGE PROCESSING

Evaluation of image data involves the handling of huge amounts of data. Thus it is crucial to work with efficient data structures and algorithms. This section details all steps from the raw image data to the two-dimensional wave number spectra.

4.1. Noise Reduction by Median Filtering

It turned out that the digitized images contained a kind of gray-level-dependent "salt and pepper" noise which was caused by a small defect in the analog digital converter of the frame buffer. This effect could be detected only after contrast enhancement but caused an increase in the noise level in the spectra. Since it is basically white noise, it shows up as an increase $\propto k^2$ in the degree of saturation of the spectra (Figure 5a).

A 3×3 median filter was used to reduce this type noise efficiently. Unlike a linear convolution-type filter which simply multiplies the Fourier transform by some factor, a median filter is especially suitable to remove isolated distorted pixels in an image which increase the white noise level in the spectrum. Though the median filter is not directionally sensitive, it basically filters out

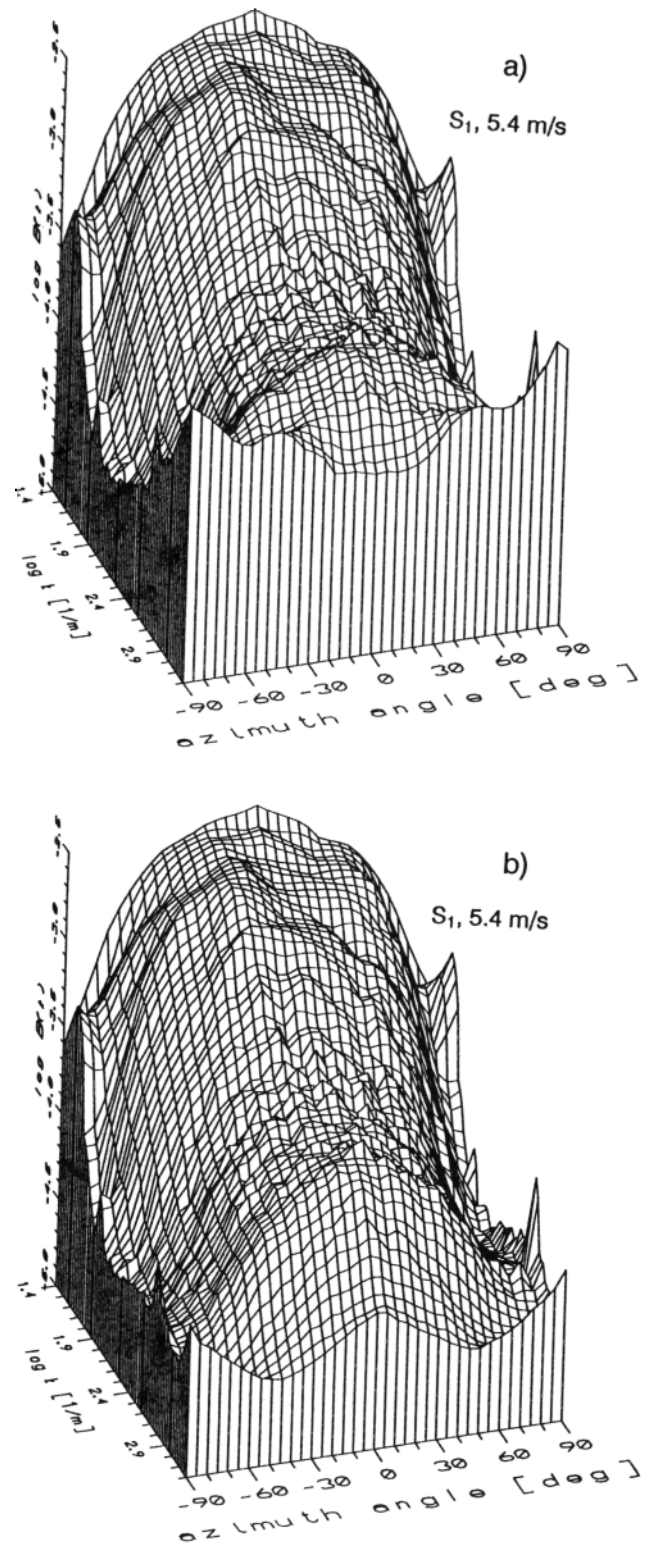


Fig. 5. Noise removal by median filtering: (a) mean wave number spectrum of the original wave image sequence ($U_{10} = 5.4 \text{ ms}^{-1}$); (b) wave number spectrum of the median-filtered sequence. Spectra are shown as degree of saturation $B(k) = S(k)k^2 = F(k)k^4$ with a logarithmic axis.

the increasing spectral densities at high wave numbers in the cross-wind direction, which are reduced by almost a decade; in the along-wind direction, however, the spectral density is damped at most by 40%. (Fig-

ure 5b). This result clearly demonstrates that the median filter effectively removes the noise, but does not significantly damp high wave numbers. The damping by 40% is thus only an upper limit, since the median filter probably also removed some noise in the along-wind direction.

4.2. Subtraction of Least Squares Plane

The images contain waves with wavelengths larger than the imaged sector. Without any corrections, spectral leakage into the low wave number range would occur. In order to diminish this effect, each image was fitted by a plane with a least squares algorithm. The fitted plane was subtracted from the image. In this way, a zero-mean image is obtained, and the mean slope of large scale waves and the intensity gradient due to the illumination is compensated for.

4.3. Windowing

Windowing is especially important for two-dimensional data, since a rectangular window results in a star-like pattern in the spectra along the principal axes. We used a cos window (Hanning window).

4.4. Two-Dimensional FFT

Because the intensity levels in the images are quantized with only 8-bit resolution, a 16-bit integer FFT algorithm provided sufficient accuracy. Whenever overflow occurred, the data were scaled down by a factor of 2 (block-floating). A separable radix-two FFT algorithm was used, which first transformed the rows and then the columns. The algorithm transforms the image in the frame buffer of the image processing system and is vectorized in the sense that all rows and columns are transformed simultaneously [Jähne, 1989a]. This procedure significantly reduces the overhead of the algorithm and thus avoids any trivial multiplication by checking the multiplication factor for trivial values such as 1, -1, i , or $-i$, before the butterfly operation is applied to a vector. The whole image evaluation including the steps described in sections 4.1.-4.4. took about 1 min per image.

4.5. Remapping the Power Spectra on a $(\ln k, \Theta)$ Grid

The mean power spectra are remapped on the $(\ln k, \Theta)$ grid, which was introduced in section 2.3. The mapping itself is done by bilinear interpolation of the spectral densities between the four nearest neighbors on the Cartesian grid.

4.6. Addition of Along- and Cross-Wind Slope Spectra

The last step yields the total slope spectrum by addition of the along- and cross-wind slope spectra according to (4). Figure 6 shows that there are actually cross-wind traveling waves present which would have been lost without measuring the cross-wind slope spectrum.

5. RESULTS

5.1. Summary

All measurements were obtained in the large wind-wave facility of Delft Hydraulics at a fetch of 100 m, 14°C water temperature, and neutral stability of the air flow. The friction velocities have been measured by KNMI with a pressure anemometer [Oost, 1983]. The experimental conditions are summarized in Table 2.

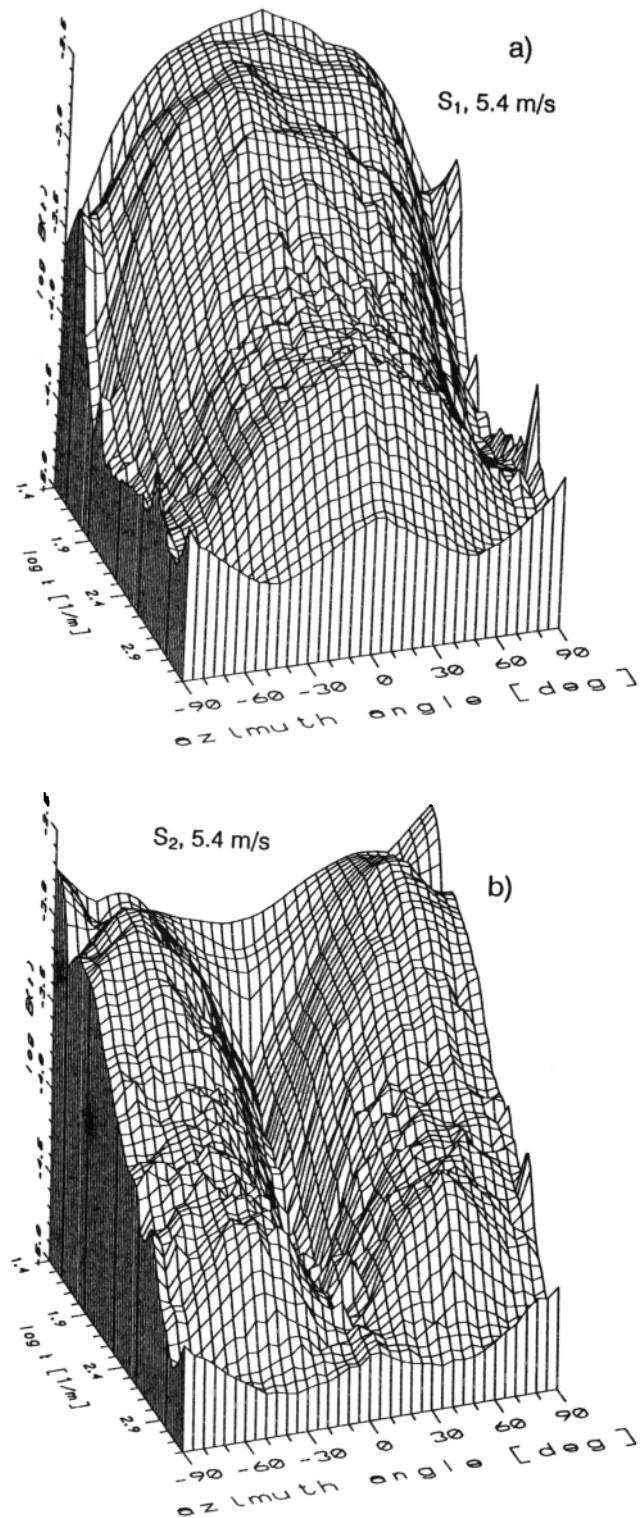


Fig. 6. a) Along-wind and (b) cross-wind slope spectra at 5.4 ms^{-1} wind speed. The corresponding total slope spectrum as the sum of both is shown in Fig. 8c.

From the measured friction velocities, equivalent wind speeds at a height of 10 ms^{-1} , U_{10} , have been calculated. In the following we refer to these values. Two-dimensional wave number spectra are available at seven wind speeds from 2.7 to 17.2 ms^{-1} . Wave slope frequency spectra were obtained simultaneously with a

TABLE 2. Summary of the Evaluated Two-Dimensional Wave Number Spectra Measured in the Delft Wind-Wave Facility at a Fetch of 100 m

Reference Wind Speed U_r (ms^{-1})	Friction Velocity u_* , (ms^{-1})	Wind Speed 10 m U_{10} (ms^{-1}) ^a	Number of Frames ^b
2.12	0.073	2.7	95, 38
3.08	0.100	3.9	138, 113
4.20	0.140	5.4	116, 130
5.62	0.205	7.3	115, 109
6.78	0.269	8.9	104, 122
9.06	0.424	12.2	119, 119
12.4	0.722	17.2	152, 135

^aEstimated from the measured friction velocities assuming a logarithmic wind profile.

^bFirst figure along-wind, second cross-wind slope spectra.

laser slope gauge (Figure 7). These data are discussed in another paper (B. Jähne, in preparation, 1990) and are used here only to be compared with the two-dimensional wave number spectra. The vertical lines in Figure 7 in-

dicate the sector of the spectrum which corresponds to the wave number spectra. All wave number spectra are summarized in Figure 8. The wave number spectra are shown in a three-dimensional plot on a $(\ln k, \Theta)$ grid and with a logarithmic scale for the degree of saturation $B(k)$. The plots cover wave numbers from 26.5 to 1701 m^{-1} (wavelengths from 23.6 cm down to 0.36 cm) and an angular range of $\pm 90^\circ$. The full angular range of 360° cannot be resolved from single images, since they contain a 180° ambiguity, i.e., waves traveling with and against the wind direction cannot be distinguished.

At the lowest wind speed (Figure 8a) of 2.7 ms^{-1} , the dominant wave is just within the measured wave number range. The frequency spectrum (Figure 7) gives a peak frequency of 2.8 Hz . Using the linear dispersion relation, this results in a wavelength of 20 cm in agreement with the position of the peak in the wave number spectrum. While the angular dispersion of the dominant wave is narrow it widens considerably towards smaller wavelengths. It is quite flat over a range of about $\pm 45^\circ$ with a clear tendency towards a bimodal distribution. Beyond a wavelength of 6 cm , the spectral

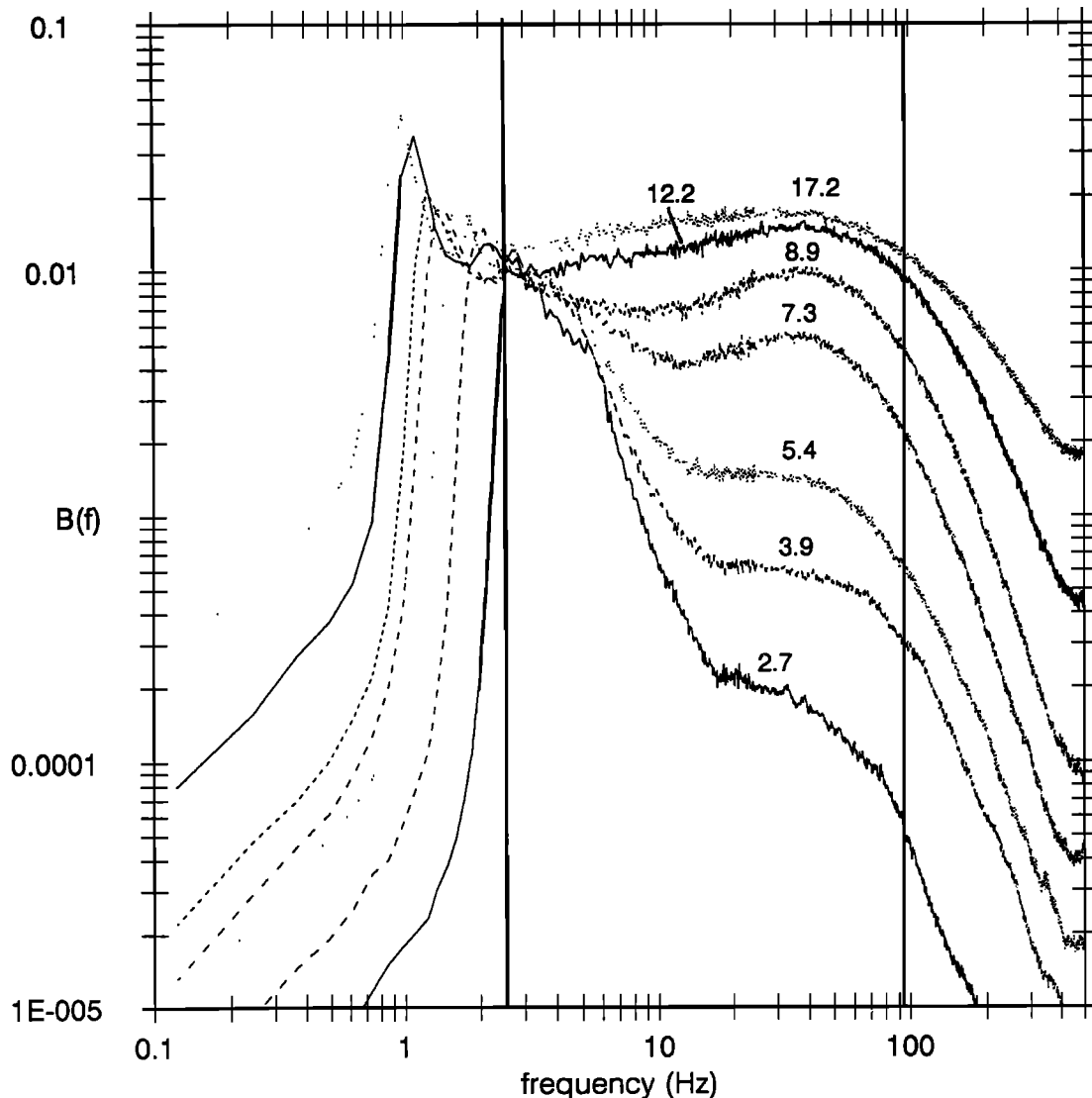


Fig. 7. Wave frequency spectra measured at the same wind speeds and about 90 m fetch with the laser slope gauge. The vertical lines mark the approximate range contained in the wave number spectra.

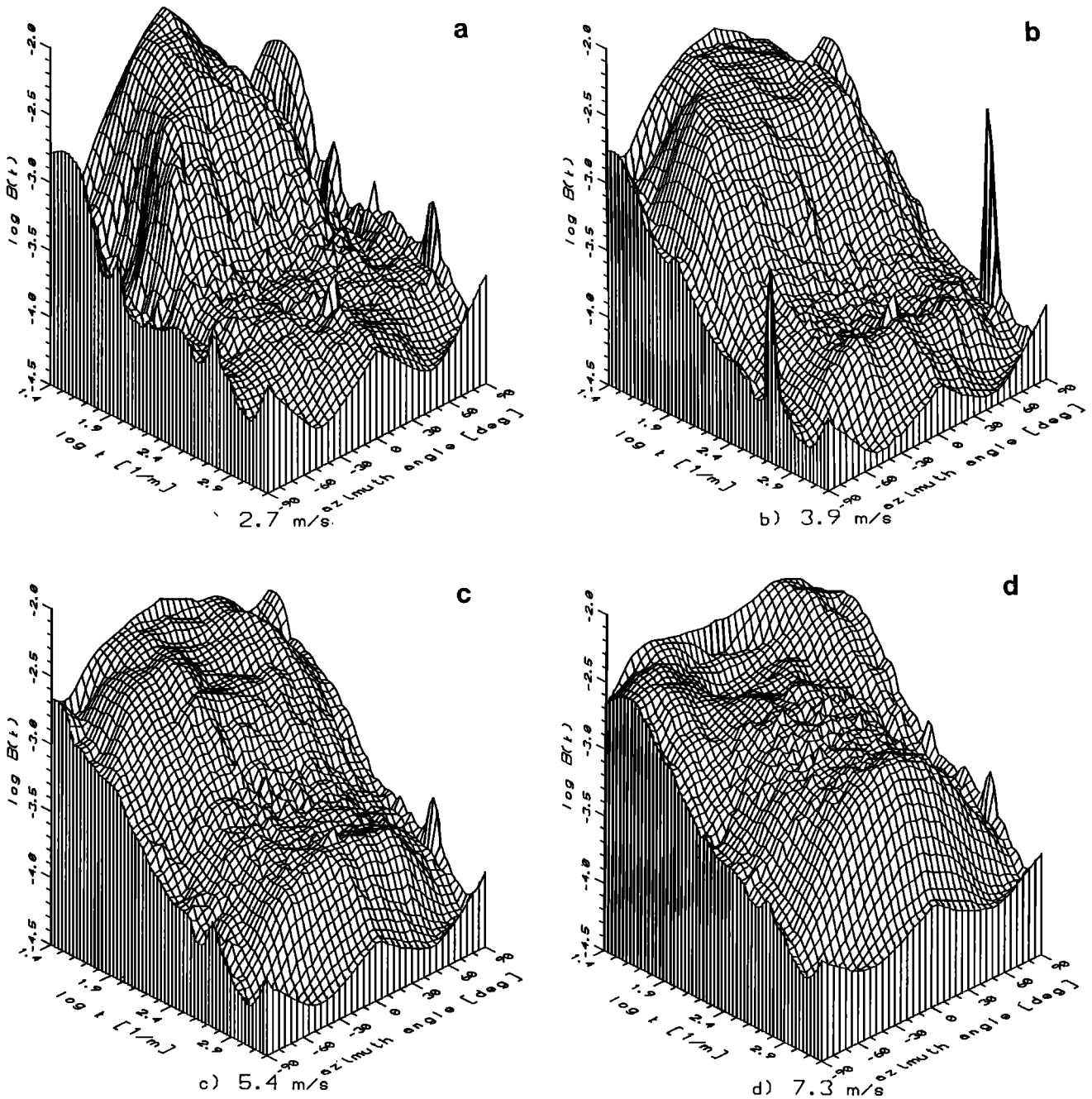


Fig. 8. Collection of all two-dimensional wave number spectra measured at 100-m fetch and represented as degree of saturation in a $(\ln k, \Theta)$ grid at wind speeds indicated.

densities drop steeply until they reach a plateau with spectral densities about 1.5 decades lower. Again, the smallest waves show a smaller angular dispersion peaking in the along-wind direction, very similar to that of the dominant wave. The different spikes at $\pm 90^\circ$ are remaining artifacts as discussed in section 3.7.

At higher wind speeds, the dominant wave is no longer contained within the measured wave number range. The features found at the lowest wind speed gradually change as the wind speed increases. The bimodal angular dispersion first becomes more pronounced, but then transforms into a unimodal distribution which becomes continuously wider. The spectral densities for wavelengths between 0.5 and 3 cm strongly increase with wind speed

and finally exceed the levels at larger wavelengths at the highest wind speed. Here, the angular dispersion is very wide. Cross-wind traveling waves show spectral densities not less than half of the values for along-wind waves.

After this general overview, a more specific and quantitative analysis of the data follows, based on k or Θ profiles extracted from the two-dimensional data.

5.2. Wave Number Dependence

Figure 9 shows profiles at 0° , 30° , and 60° to the wind direction and one integrated over all angles, i.e., the unidirectional k spectrum. At low wind speeds, the spectral shape is governed by a strong decrease towards

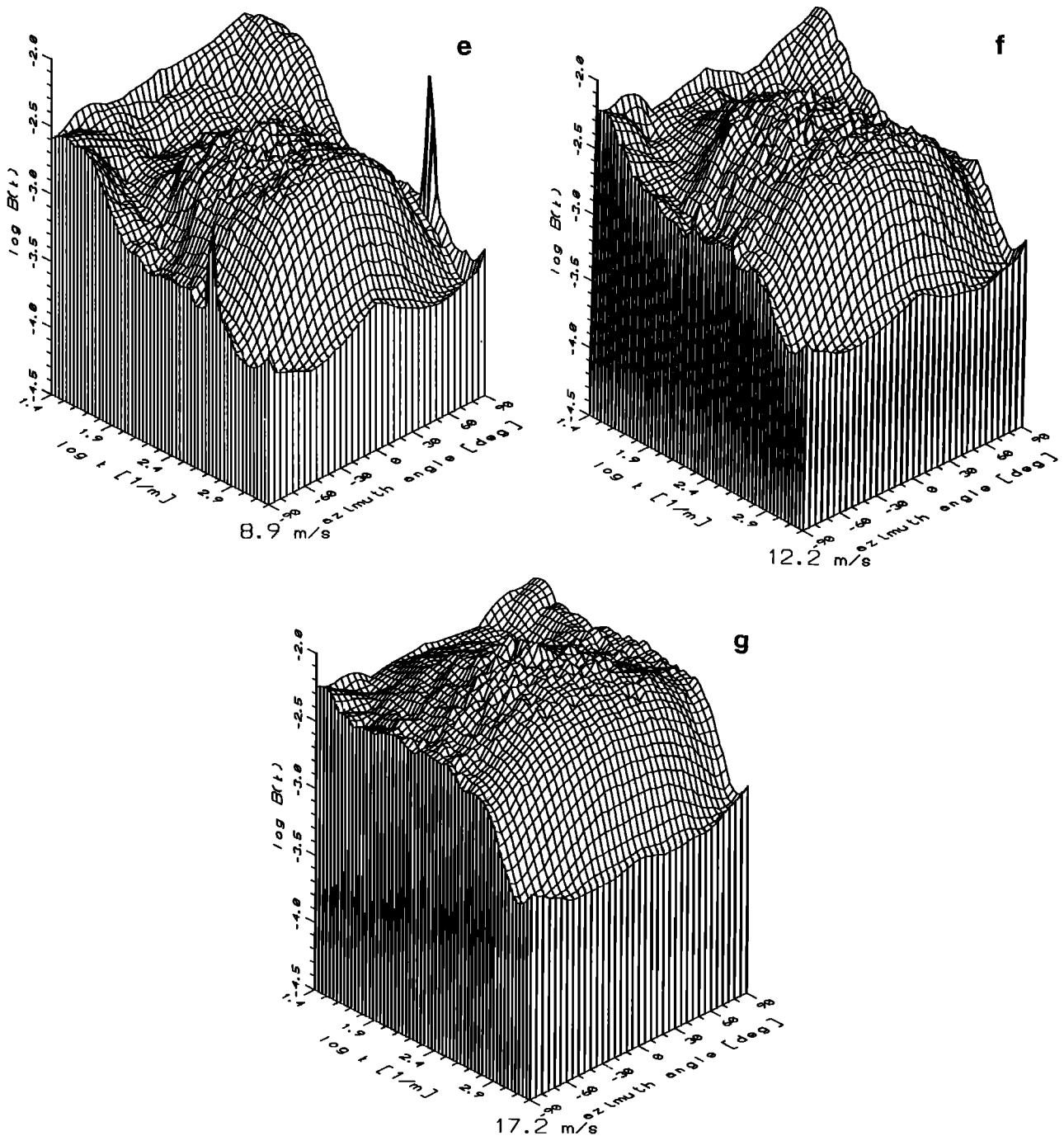


Fig. 8. (continued)

higher wave numbers, especially in the along-wind direction (Figure 9a). The profiles also show that the dominant peak is included only at the lowest wind speed of 2.7 ms^{-1} . At moderate wind speeds, only the decrease from the dominant peak is observed, while at the highest wind speeds a small gravity wave range has obviously been established. The spectral peak at 17.2 ms^{-1} is located at a frequency of 1 Hz in the frequency slope spectrum (Figure 7), corresponding to a wavelength of 1.56 m . Thus the dominant wave is separated by about one decade from the small gravity range at wavelengths from 5 to 20 cm . This should be a suf-

ficient separation of the small gravity wave range from the dominant wave, though at sea it typically has a ten times larger wavelength.

In the small gravity range, the degree of saturation increases. This increase depends on the propagation direction. While it is approximately proportional to $k^{0.6}$ for the along-wind component, it is only $\propto k^{0.35}$ in the unidirectional k spectrum. This means that these data support a $k^{-3.5}$ height spectra for wavelengths between 3 cm and 24 cm , rather than a constant degree of saturation.

In a wave number range of about $200\text{--}800 \text{ m}^{-1}$ (0.75--

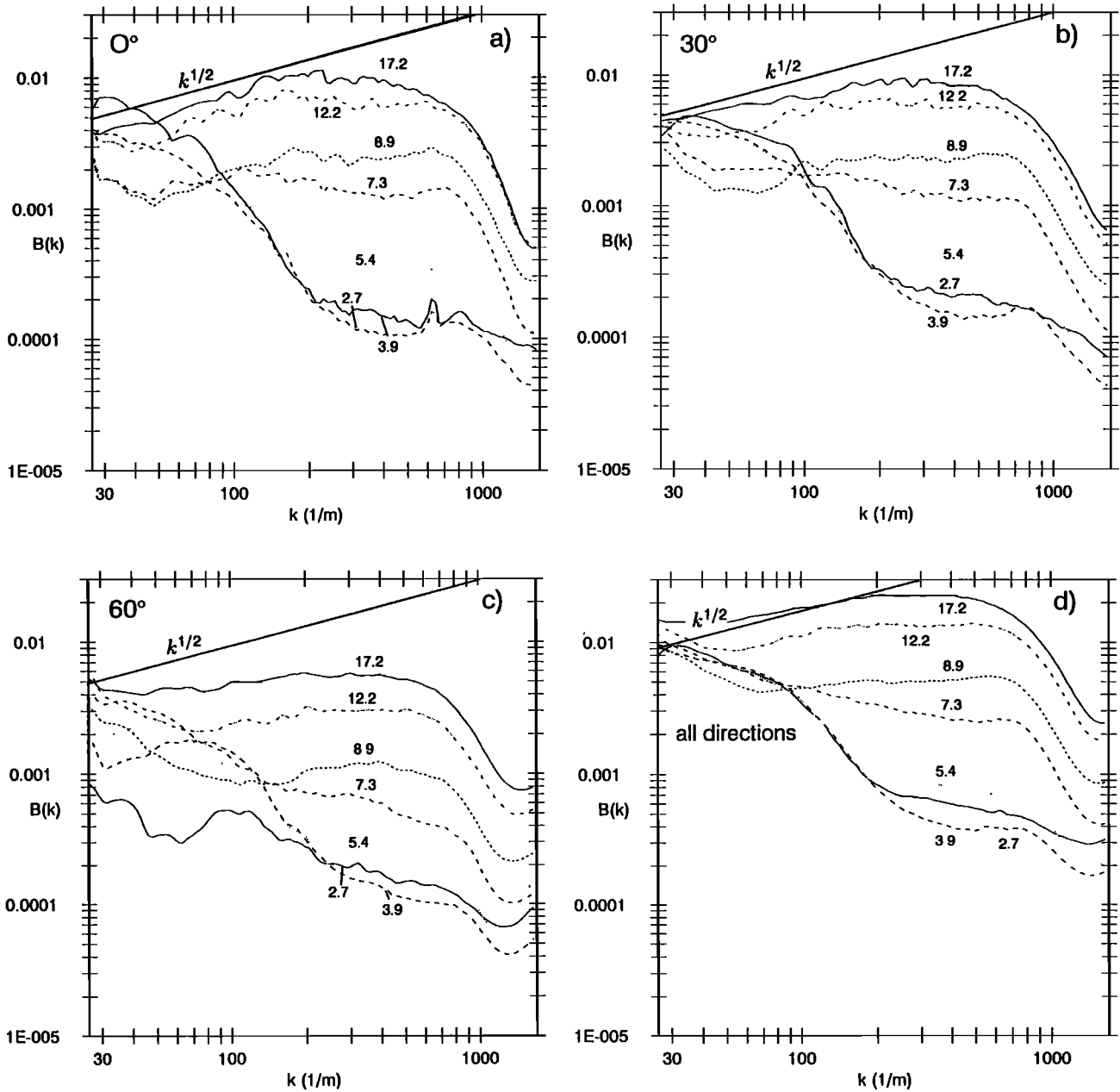


Fig. 9. Wave number spectra in different directions: (a) along-wind ($\pm 5^\circ$); (b) $30 \pm 5^\circ$; (c) $60 \pm 5^\circ$; (d) unidirectional spectra integrated over all angles; wind speeds (U_{10} in ms^{-1}) as indicated.

3 cm wavelength), a plateau is reached where the degree of saturation is basically constant in the along-wind direction. At the lowest wind speeds of 2.7 ms^{-1} and 3.9 ms^{-1} , this plateau is obviously influenced by the noise level. While in the slope frequency spectra measured with the laser gauge the spectral densities continue to decrease even at the lowest wind speeds (Figure 7), they do not do so in the wave number spectra. In contrast to the plateau in the along-wind direction, the spectral densities at 30° and 60° decrease slowly with increasing wave number. This means that the angular dispersion is getting narrower towards higher wave numbers. The unidirectional spectra (Figure 9d) show the same trend.

Beyond a wave number of 800 m^{-1} , the spectral densities fall off steeply. This cutoff is nearly independent of the wind speed. It seems to occur only at the lowest wind speeds, at a slightly higher wave number of 1000 m^{-1} . The discussion in section 3.4. has shown that the resolution limit of the images lies at 1250 m^{-1} . Thus, the strong decrease of the spectral densities beyond 800 m^{-1} seems to be a real effect, although the shape of the cutoff may be influenced by the limited resolution and the median filtering. The hypothesis of a cutoff independent of the wind speed is also supported by the slope frequency spectra (Figure 7). Here the cutoff frequency increases only slightly with wind speed from about 65 Hz at 7.3 ms^{-1} to about 100 Hz at

17.2 ms^{-1} . This comparison also shows that a cutoff at $k = 800 \text{ m}^{-1}$ is reasonable, since it leads to mean phase velocities of 50 cms^{-1} and 78 cms^{-1} , respectively. These values, including the increase in the phase velocity, are reasonable since at higher wind speeds the orbital velocities advecting the small scale waves are significantly larger.

5.3. Wind Speed Dependence

The wind speed dependence of the degree of saturation shows a remarkable change with the wave number (Figure 10). Small gravity waves are much less dependent on the wind speed than are gravity-capillary and capillary waves. The unidirectional spectral den-

sities for 6.3-cm and 12.5-cm waves are independent of the friction velocity up to a friction velocity of about 0.3 ms^{-1} , where they start increasing, in approximate proportion to the friction velocity (Figure 10c). The same pattern can be observed for the along-wind component, with the exception that the 12.5-cm waves decrease first (Figure 10a). This effect is related to the fact that at low wind speeds the 12.5-cm wave comes closer to the along-wind traveling dominant wave.

In contrast, the spectral densities of capillary-gravity and capillary waves in the wavelength range of 0.7–3 cm strongly increase with friction velocity (Figure 10b and Figure 10d). The curves are S-shaped, with the steepest increase roughly $\propto u_*^3$ at medium friction velocities.

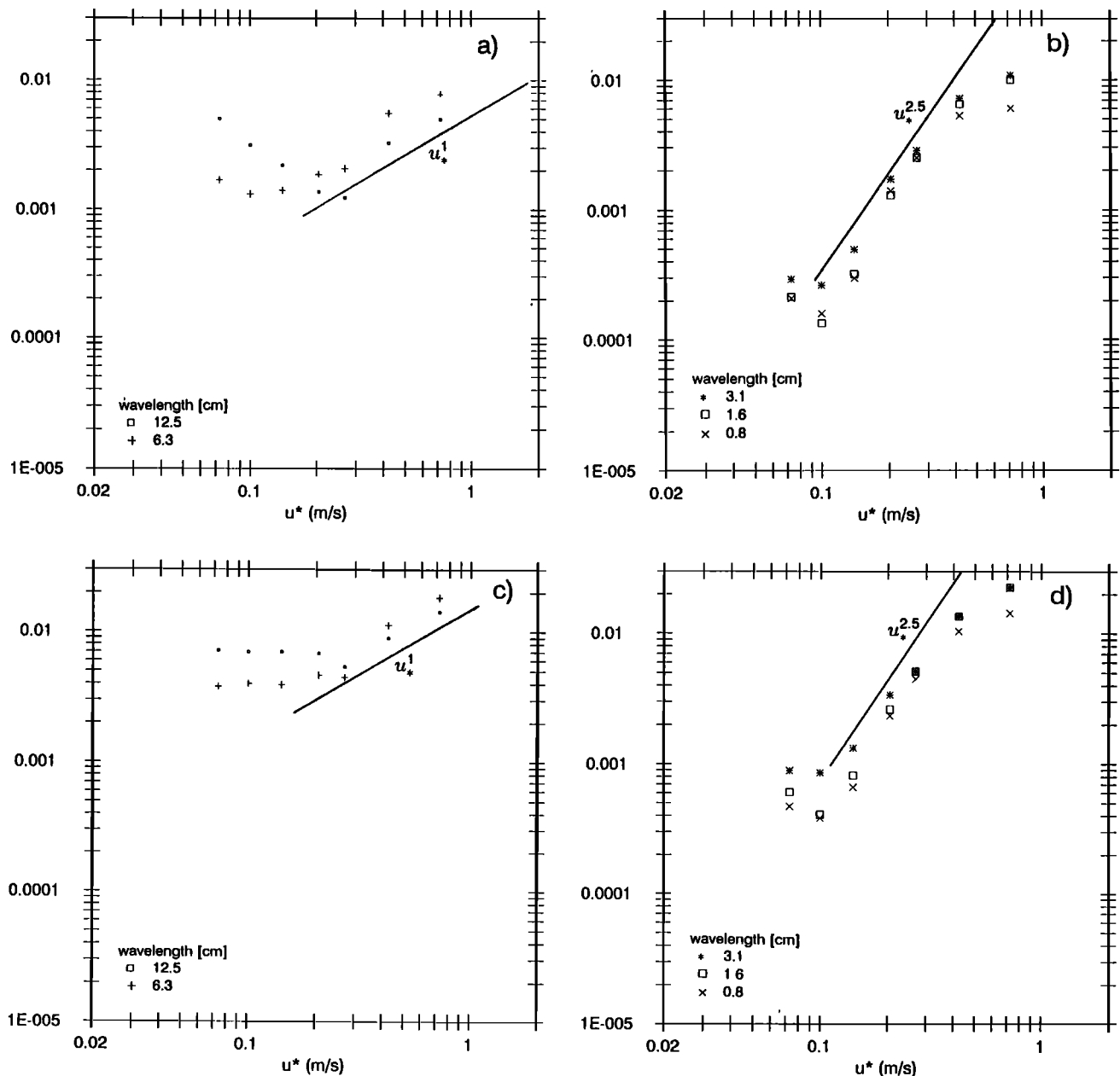


Fig. 10. Dependence of spectral densities on the friction velocity in different wave number ranges as indicated: (a) small gravity waves, along-wind; (b) gravity-capillary waves and capillary waves, along-wind; (c) small gravity waves, unidirectional; (d) gravity-capillary waves and capillary waves, unidirectional.

The mean exponents (disregarding the two lowest and the highest wind speed) are 2.5 ± 0.2 and 2.4 ± 0.2 for along-wind and unidirectional spectral densities, respectively. Very similar results have been found for slope frequency spectra in different wind-wave facilities, including the Delft facility [Jähne, 1989b].

5.4. Angular Dispersion

Finally, the two-dimensional wave number spectra allow us to investigate the angular dispersion of the waves. The significant deviations from the usually assumed \cos^p -type angular distributions have already been pointed out in the qualitative discussion of the two-dimensional spectra (Figure 8) in section 5.1. The deviations are most pronounced at low wind speeds (Figure 8a). At 2.7 ms^{-1} the dominant wave shows a narrow angular dispersion around the along-wind direction, while small gravity waves of about 6 cm wavelength establish a bimodal distribution peaked at about $\pm 45^\circ$. Except for the higher background due to the higher noise level, the angular dispersion of the capillary waves is very similar to that of the dominant wave.

These features in the angular dispersion suggest that two processes determine the wave number spectra at this wind speed. First, the capillary waves seem to be generated by steep dominant gravity waves than directly by the wind. The observation that capillary waves occur as bursts of short, steep wave trains [Jähne, 1989b] supports this hypothesis. Secondly, the bimodal distribution of small gravity waves indicates that the dominant waves decompose by a two-dimensional instability process.

At higher wind speeds, the angular dispersion gradually becomes more uniform. At 5.4 ms^{-1} there are still some indications of a bimodal distribution now shifted towards larger wavelengths (Figure 8c). In the gravity-capillary range the distribution is still flatter than with a \cos^p -type distribution.

6. CONCLUSIONS AND OUTLOOK

Viewed against the background of the theoretical discussion in section 2.4., the wave number spectra show a number of interesting and surprising features:

1. In the small gravity range (3–24 cm wavelength) and at higher wind speeds, the spectral densities behave approximately as expected from theories balancing the different terms of the energy flux in the gravity wave field. The height wave number spectrum goes approximately with $k^{-3.5}$ and u_* . However, this does not mean that the data verify these theories. Inferring the energy balance from the spectral densities is rather an underdetermined inverse problem as is shown by the coinciding results of the theories based on quite different assumptions [Phillips, 1985 and Kitaigorodskii, 1983]. At lower wind speeds the dominant waves have wavelengths too short, even in the 100-m Delft facility. Thus the small gravity wave range is "contaminated" by them, and an equilibrium range is not established.

2. The wave number spectra change significantly for waves shorter than 3 cm ($k \approx 200 \text{ m}^{-1}$). Then the height wave number spectra goes with k^{-4} and

strongly depends on the friction velocity ($\propto u_*^{2.5}$). It is worthwhile to note that these changes do not occur right at the transition from gravity to capillary waves at $\lambda = 1.73 \text{ cm}$ or $k = 363 \text{ m}^{-1}$, respectively, but at a wave number less than 150 m^{-1} . The significant change in the dependence on the friction velocity is a clear indicator that the energy balance for these shorter waves differs from the energy balance for gravity waves. The $u_*^{2.5}$ -dependence comes close to the u_*^3 -dependence of the wind input term. Consequently, the dissipation term seems to be only weakly dependent on the mean spectral energy density in this range.

3. The wind speed independent cutoff is another remarkable feature. This experimental fact stands in clear contrast to the assumption that the cutoff is determined by a balance between the wind input and viscous dissipation as discussed in section 2.4. Since all energy fluxes increase with wind speed except for viscous dissipation, a wind-speed-independent cutoff indicates that viscous dissipation seems to play only a minor role.

There is one direct observation from the wave images that were obtained supporting this idea. While at low wind speeds wave trains of capillary waves may be 10–20 wavelengths long, they range over only a few wavelengths at higher wind speeds [Jähne *et al.*, 1987]. Thus, the energy flux is very large at small wavelengths and the overall attenuation rate at high wind speeds is certainly higher than 0.3. In comparison, viscous dissipation is a weak process even at these small wavelengths. A wave with a wavelength of 7 mm has an attenuation rate of about 0.01 and 0.03 at a clean and a surface film covered surface, respectively [Phillips, 1980]. This rate is very low compared to the observed attenuation of the wavelets. This obvious discrepancy directs attention to other dissipation mechanisms such as turbulent damping. Especially important are more detailed studies on the propagation of capillary waves in the highly sheared current of the viscous boundary layer.

4. The data at low wind speed indicate that direct generation of capillary waves by steep unstable gravity waves seems to be a significant energy transfer mechanism. By its very nature, as a single-step process, it should be more efficient than a multistep cascade process.

In conclusion, the two-dimensional wave number spectra give some first insight into the energy balance of small scale waves, but it is not readily and unambiguously deferrable. By analyzing only mean wave number spectra, most information contained in the images is disregarded. Actually, image sequences from the waves contain the complete spatiotemporal information on the wave field, except for the limitations imposed by the size of the images. Thus, a promising research avenue opens up for other kinds of image sequence processing to investigate directly the energy cycling in the wave field. Tracing of individual wavelets should be one way to determine their mean lifetime and coherency lengths, parameters that are not only of importance for a better understanding of water wave physics, but also to the radar remote sensing community. Digital image processing nowadays offers the tools for such detailed investigation of wave image sequences.

Acknowledgments. The authors would like to express their sincere thanks to their Dutch colleagues for the excellent and efficient cooperation in the frame of the VIERS project. The following organizations participated: The Royal Netherlands Meteorological Institute (KNMI), the Physics and Electronics Laboratory of the Netherlands Organization for Applied Research (TNO), the Technical University of Delft, and Delft Hydraulics. Financial support by the State of Baden-Württemberg (Federal Republic of Germany), the German Science Foundation, the European Community (twinning contract), and the Director's office of Scripps Institution of Oceanography is gratefully acknowledged. Part of the data evaluation has also been supported by a grant from the California Space Institute. The authors would also like to thank two anonymous reviewers for their detailed and helpful comments.

References

- Alpers, W., and H. Hühnerfuss, The damping of ocean waves by surface films: a new look at an old problem, *J. Geophys. Res.*, *94*, 6251-6265, 1989.
- Banner, M. L., I. S. F. Jones, and J. C. Trinder, Wavenumber spectra of short gravity waves, *J. Fluid Mech.*, *198*, 321-344, 1989.
- Cox, C., Measurements of slopes of high frequency waves, *J. Mar. Res.*, *16*, 199-225, 1958.
- de Loor, G. P., Tower-mounted radar backscatter measurements in the North Sea, *J. Geophys. Res.*, *88*, 9785-9791, 1983.
- Donelan, M. A., and W. J. P. Pierson, Radar scattering and equilibrium ranges in wind-generated waves with application to scatterometry, *J. Geophys. Res.*, *92*, 4971-5029, 1987.
- Glazman, R. E., and S. H. Pilorz, Effects of sea maturity on satellite altimeter measurements, *J. Geophys. Res.*, *95*, 2857-2870, 1990.
- Glazman, R. E., G. G. Pihos, and J. Ip, Scatterometer wind speed bias induced by the large-scale component of the wave field, *J. Geophys. Res.*, *93*, 1317-1328, 1988.
- Hughes, B. A., H. L. Grant, and R. W. Chappel, A fast response surface-wave slope meter and measured wind-wave moments, *Deep Sea Res.*, *24*, 1211-1223, 1977.
- Jähne, B., *Digitale Bildverarbeitung*, Springer-Verlag, New York, 1989a.
- Jähne, B., Energy balance in small-scale waves — an experimental approach using optical slope measuring technique and image processing, *Radar Scattering from Modulated Wind Waves*, edited by G. Komen and W. Oost, pp. 105-120, Kluwer, Boston, 1989b.
- Jähne, B. and S. Waas, Optical measuring technique for small scale water surface waves, *Advanced Optical Instrumentation for Remote Sensing of the Earth's Surface*, SPIE conference proceedings 1129, pp. 122-128, Washington, 1989.
- Jähne, B., K. O. Münnich, R. Böisinger, A. Dutzi, W. Huber, and P. Libner, On the parameters influencing air-water gas exchange, *J. Geophys. Res.*, *92*, 1937-1949, 1987.
- Keller, W. and B. L. Gotwols, Two-dimensional optical measurement of wave slope, *Appl. Opt.*, *22*, 3476-3478, 1983.
- Keller, W. C., W. J. Plant, and D. E. Weissman, The dependence of X band microwave sea return on atmospheric stability and sea state, *J. Geophys. Res.*, *90*, 1019-1029, 1985.
- Kinsman, B., *Wind Waves, Their Generation and Propagation on the Ocean Surface*, Prentice-Hall, Englewood Cliffs, 1965.
- Kitaigorodskii, S. A., On the theory of the equilibrium range in the spectrum of wind-generated gravity waves, *J. Phys. Oceanogr.*, *13*, 816-827, 1983.
- Komen, G. J. and W. A. Oost, *Radar Scattering from Modulated Wind Waves*, Kluwer, Boston, 1989.
- Lange, P. A., B. Jähne, J. Tschiersch, and J. Ilmberger, Comparison between an amplitude-measuring wire and a slope-measuring laser water wave gauge, *Rev. Sci. Instrum.*, *53*, 651-655, 1982.
- McGoldrick, L. F., Resonant interactions among capillary-gravity waves, *J. Fluid Mech.*, *21*, 305-331, 1965.
- Oost, W. A., The pressure anemometer — an instrument for adverse circumstances, *J. Clim. Appl. Meteorol.*, *12*, 2075-2084, 1983.
- Phillips, O. M., The equilibrium range in the spectrum of wind-generated waves, *J. Fluid Mech.*, *4*, 426-434, 1958.
- Phillips, O. M., *The Dynamics of the Upper Ocean*, Cambridge University Press, New York, 1980.
- Phillips, O. M., Spectral and statistical properties of the equilibrium range in wind-generated gravity waves, *J. Fluid Mech.*, *156*, 505-531, 1985.
- Plant, W. J., General discussion on the energy balance in short wind waves, *Radar Scattering from Modulated Wind Waves*, edited by G. Komen and W. Oost, pp. 249-251, Kluwer, Boston, 1989.
- Rosenthal, W., Derivation of Phillips α -parameter from turbulent diffusion as a damping mechanism, *Radar Scattering from Modulated Wind Waves*, edited by G. Komen and W. Oost, pp. 81-87, Kluwer, Boston, 1989.
- Schroeder, L. C., D. H. Boggs, G. Dome, I. M. Halberstam, W. L. Jones, W. J. Pierson, and F. J. Wentz, The relationship between wind vector and normalized radar cross section used to derive Seasat-A satellite scatterometer winds, *J. Geophys. Res.*, *87*, 3318-3336, 1982.
- Shemdin, O. H. and L. D. McCormick, Saxon-I '88 Field experiment data survey report, Ocean Research and Engineering, Pasadena, Calif., ORE 89-2, Office of the Chief of Naval Research, 1989.
- Shemdin, O. H., H. M. Tran, and S. C. Wu, Directional measurements of short ocean waves with stereophotography, *J. Geophys. Res.*, *93*, 13891-13901, 1988.
- Stilwell, D., Directional energy spectra of the sea from photographs, *J. Geophys. Res.*, *74*, 1974-1986, 1969.
- Tober, G., R. C. Anderson, and O. H. Shemdin, Laser instrument for detecting water ripple slopes, *Appl. Opt.*, *12*, 788-794, 1973.
- van Halsema, E., B. Jähne, W. A. Oost, C. Calkoen, and P. Snoeij, First results of the VIERS-1 experiment, *Radar Scattering from Modulated Wind Waves*, edited by G. Komen and W. Oost, p. 49-57, Kluwer, Boston, 1989.

B. Jähne, Scripps Institution of Oceanography, Physical Oceanography Research Division, University of California, San Diego, La Jolla, CA 92093.

K. S. Riemer, Institut für Umweltphysik, University, Im Neuenheimer Feld 366, D-6900 Heidelberg, Federal Republic of Germany.

(Received August 23, 1989;
accepted February 5, 1990.)